Marine Geodesy, 27: 199–220, 2004

ISSN: 0149-0419 print / 1521-060X online
DOI: 10.1080/01490410490465643

Taylor & Francis
Taylor & Francis Group

Jason Microwave Radiometer Performance and On-Orbit Calibration

SHANNON BROWN
CHRIS RUF

University of Michigan

STEVE KEIHM
AMI KITIYAKARA

Jet Propulsion Laboratory

Results are presented from the on-orbit calibration of the Jason Microwave Radiometer (JMR). The JMR brightness temperatures (TBs) are calibrated at the hottest and coldest ends of the instrument's dynamic range, using Amazon rain forest and vicarious cold on-Earth theoretical brightness temperature references. The retrieved path delay values are validated using collocated TOPEX Microwave Radiometer and Radiosonde Observation path delay (PD) values. Offsets of 1–4 K in the JMR TBs and 8–12 mm in the JMR PDs, relative to TMR measurements, were initially observed. There were also initial TB offsets of 2 K between the satellite's yaw state. The calibration was adjusted by tuning coefficients in the antenna temperature calibration algorithm and the antenna pattern correction algorithm. The calibrated path delay values are demonstrated to have no significant bias or scale errors with consistent performance in all nonprecipitating weather conditions. The uncertainty of the individual path delay measurements is estimated to be 0.74 cm ± 0.15, which exceeds the mission goal of 1.2 cm RMS.

Keywords calibration, microwave radiometer, JMR, TMR, satellite, path delay

The Jason-1 satellite is a joint venture by NASA and the French space agency Centre National d'Etudes Spatiales (CNES). It is designed to produce global maps of ocean surface topography to determine the general circulation of the ocean and to understand its role in the Earth system. It was launched on 7 December 2001 from Vandenberg Air Force Base. Jason carries five instruments. The mission critical instruments are the Poseidon-2 radar altimeter and the Jason Microwave Radiometer (JMR). JMR is included to measure the electrical range delay of the altimeter signal through the troposphere due to water vapor and cloud liquid water (henceforth referred to as path delay). If the path delay (PD) in the altimeter signal is left uncorrected, errors in the range measurement will be on the order of 3–45 cm (Keihm et al. 1995).

Jason-1 is a follow-on mission to the highly successful TOPEX/Poseidon (T/P) mission, which was launched on 10 August 1992. The Topex Microwave Radiometer (TMR) has been determining the path delay correction of the atmosphere to the 1.1 cm level of accuracy for over 10 years (Keihm et al. 2000). The T/P mission follows a lineage of precise satellite

Received 6 October 2003; accepted 25 January 2004.
Address correspondence to Shannon Brown, University of Michigan, 2455 Hayward St., Ann Arbor, MI 48109-2143. E-mail: brownst@engin.umich.edu

altimetry missions dating back to 1986 when Geosat was launched. GFO, the Geosat follow on, and the European ERS-1 and ERS-2 satellites with the Envisat follow-on include microwave radiometers that provide vapor-related range corrections. A summary of the retrieval techniques and accuracy of the PD range corrections of these instruments can be found in Ruf et al. (1995) and Keihm et al. (1995). A summary of the TMR performance and calibration is provided in the section on the Jason-1/TOPEX Tandem Mission.

Microwave radiometers can determine the integrated water vapor content of the atmosphere by measuring the intensity of the microwave emission near the 22.235 GHz water vapor absorption line. In addition to the emission by water vapor, the microwave brightness temperature (TB) measured by JMR will depend on surface roughness and foaming due to winds, ocean temperature and salinity, and cloud liquid water (Ulaby et al. 1986). JMR operates at 18.7, 23.8, and 34.0 GHz with a nadir-viewing geometry that is coaligned with the altimeter. The JMR antenna is an offset parabolic reflector with partial blockage from the feedhorn and has a projected aperture of 79 cm. The partial blockage from the feedhorn causes the sidelobe fractions to be higher than if there were no blockage. The 18.7 and 34.0 GHz channels are included to determine the excess brightness in the 23.8 GHz TB due to surface winds and clouds. The combination of the three JMR channels ensures an accurate retrieval of the water vapor signal in all nonprecipitating weather conditions.

Summary of JMR Performance Requirements

The primary goal of the Jason-1 mission is measurement of the sea surface topography at the same level of performance as T/P. This will provide a continuous time series of high precision ocean measurements from 1992 to the present which will be invaluable for the study of global circulation and climatology. A secondary mission goal is the generation of nonvalidated real-time data in preparation for operational data production (Menard and Haines 2001). This will pave the way for the Jason-2 mission, which will provide operational oceanographic data for use by NOAA and others. The Jason-1 altimeter measurements are required to have an uncertainty of measurement less than ± 4.2 cm. JMR is required to have a wet tropospheric path delay retrieval uncertainty less than ± 1.2 cm with a goal of ± 1.0 cm (Jason-1 Project 2001). To achieve these requirements, an extensive Jason-1 ground-based calibration campaign was conducted for the first eight months of the mission.

Description of JMR Instrument Algorithms

The retrieval of path delay from the raw JMR receiver measurements is divided into three levels of processing. Level 1a processing determines the antenna temperature, Level 1b processing determines the brightness temperature, and Level 2 processing determines the PD.

Level 1a processing converts the raw digital counts to antenna temperatures using a noise-diode calibration method (Kitiyakara 2002). The Level 1a processing also corrects for hardware losses from the system components between the antenna and the internal calibration reference. The antenna temperature is given by

$$T_A = T_N \gamma_X + K_R T_R + K_{FH} T_{FH}, \tag{1}$$

where T_{FH} and T_R are the feedhorn and reference load temperature, K_{FH} and K_R account for all loss-dependent offsets proportional to T_{FH} and T_R, T_N is the calibration noise source

noise temperature, and

$$\gamma_X = \frac{X_A - X_R}{X_N - X_A}, \tag{2}$$

where X_A is the radiometer output count from the antenna position (noise source off), X_R is the radiometer output count from the reference position, and X_N is the radiometer output count from the antenna position with the noise source on. The power from the noise diode has a temperature dependency which is corrected before being used in (1) (Stum et al. 2001a).

The Level 1b processing employs the antenna pattern correction (APC) algorithm (Stum et al. 2001b) which converts the measured antenna temperatures for each frequency to main beam brightness temperatures (TB) by inverting the antenna gain pattern to remove on-earth and off-earth side lobe contamination. This is given by

$$TB = \frac{T_A - bT_E - cT_C}{1 - b - c}, \tag{3}$$

where T_A is the antenna temperature, T_E is the effective on-Earth sidelobe brightness temperature, T_C is the effective cosmic background brightness temperature, b is the fraction of the power from the on-Earth sidelobes, and c is the fraction of the antenna gain pattern that views the cosmic background. A derivation of Equation 3 can be found in Janssen et al. (1995). The effective on-Earth sidelobe brightness temperature for each frequency, given by

$$T_E(f) = d_0(f, lat) + d_1(f, lat)T_A(f) + d_2(f, lat)T_A(f)^2, \tag{4}$$

is estimated using a quadratic function of the antenna temperature with coefficients dependent upon frequency (f) and latitude (lat). The Level 1b processing also employs an along-track averaging algorithm to generate footprints for the 23.8 and 34.0 GHz channels that are similar in size to the footprint of the 18.7 GHz channel (Stum et al. 2001b). The along-track averaged brightness temperatures from the three channels are then used to retrieve the wet tropospheric path delay in the Level 2 processing.

The path delay algorithm is a two-step statistical inversion. In the first step, an initial estimate of PD is made using coefficients valid for the entire range of path delay values. In the second step, the final PD is determined using coefficients stratified in PD, where the proper coefficients are chosen based on the initial PD estimate. The motivation for this algorithm can be found in Keihm et al. (1995). The inversion algorithm is of the form,

$$\begin{aligned} PD = {} & c_0(W, PD_{\text{int}}) + c_{18}(W, PD_{\text{int}}) \ln(280 - TB_{18.7}) \\ & + c_{23}(W, PD_{\text{int}}) \ln(280 - TB_{23.8}) + c_{34}(W, PD_{\text{int}}) \ln(280 - TB_{34.0}). \end{aligned} \tag{5}$$

The coefficients for the retrieval algorithm are dependent on surface wind speed (W) as estimated from the TBs and an initial estimate of the path delay (PD_{int}) made using global coefficients (unstratified in PD).

The coefficients for the algorithms that are included in the three levels of processing are determined prelaunch and require adjustments on-orbit. Specifically, the coefficients in Equations 1, 3, and 5 are adjusted. The on-orbit calibration process described here attempts to correct both TB and PD offsets by determining the source of the error and adjusting the proper coefficients.

Summary of the JMR cal/val Approach

The calibration of JMR is divided into two parts. The first part is the calibration of the JMR brightness temperatures and the removal of any correlation between the physical temperature of the hardware and the TBs. The second part is the validation of the retrieved path delays. By first calibrating the TBs independently from PD, errors in the PD retrieval that are related to the sensor calibration are separated from those related to the geophysical inversion algorithm.

The dynamic range of brightness temperatures that JMR encounters when viewing the Earth ranges from ∼125–150 K (across the three channels) over dry, cloud-free, calm ocean surfaces to ∼300 K over hot near blackbody land surfaces. The calibration of JMR TBs is most accurate if compared to reference brightness temperature targets at both ends of the TB range encountered while viewing the Earth. A vicarious cold reference for each frequency, representing a statistical lower bound on brightness temperature, is used to anchor the TB calibration at the cold end of the TB range. Hot blackbody targets over the Amazon rain forest are used to anchor the TB calibration at the hot end of the TB range.

Another component of the TB calibration is removal of any residual correlation of TB with instrument physical temperatures. The space environment can create significant thermal variations in the radiometer hardware and temperature gradients between the components exposed to the space environment and the internal components. Accurate conversion from raw voltage counts to antenna temperature must take into account the temperature dependent loss from the components between the antenna and the internal calibration reference. A hardware radiative transfer model and prelaunch thermal-vacuum testing were initially used to estimate corrections for the front-end hardware losses in the JMR Level 1a algorithm. Prelaunch testing is not able to duplicate all thermal conditions that the spacecraft will encounter while in orbit. Thus, the front-end thermal loss coefficients in Equation 1 are adjusted on-orbit to remove any residual correlations between JMR brightness temperature and the temperature of various hardware components.

The second part of the JMR calibration is the validation of the path delay retrieval. The path delay is validated using collocated TMR path delay values and time and space coincident Radiosonde Observation (RaOb) derived path delay values. After calibration there should be no bias between the JMR PDs and the TMR and RaOb PDs. This will ensure altimeter retrievals with minimum uncertainty and a continuous TMR/JMR data set. It is also essential that there is no scale error in the JMR PD retrieval, since errors that scale with path delay will cause errors in the ocean height retrieval that are correlated over large (zonal) spatial scales.

The JMR calibration is adjusted by changing three sets of coefficients in the calibration processing algorithms. The off-Earth side lobe fractions (c-fractions) are adjusted in the antenna pattern correction (APC) algorithm (Equation 3). Second, the front-end loss coefficients, K_R and K_{FH}, and the effective noise diode brightness, the temperature dependency of T_N, are adjusted in the antenna temperature calibration algorithm (Equation 1). Any remaining bias or scale error in the JMR PD retrieval is adjusted by changing the coefficients in the path delay retrieval algorithm (Equation 5).

Calibration/Validation Methodology

Jason-1/Topex Tandem Mission

The Jason-1 satellite was placed in a virtually identical orbit with TOPEX/Poseidon during the calibration phase of the mission, with only a 70-second displacement. This has afforded unprecedented accuracy in the intercalibration of the two instruments by removing virtually

all spatial and temporal decorrelation. The common, calibration phase orbit is inclined at 66.04° with a 9.9156-day repeat cycle. Each ~ 10-day cycle is divided into 254 passes. The orbital speed is 7.2 km/s which gives a 5.8 km/s ground track speed (Jason-1 project 2001). JMR and TMR both have a 1-second integration time.

The emphasis on TMR comparisons was motivated by two factors. First, the 10+ year TMR PD data archive has demonstrated accuracy comparable to any other satellite or ground-based benchmark (Keihm et al. 2000). Second, the intercalibration of JMR to TMR ensures continuity in the quality of the tropospheric correction for global altimetry data over the combined lifetimes of TOPEX/Poseidon and Jason.

The TOPEX Microwave Radiometer was calibrated using various sources of ground truth during the first six months of its mission in 1992 (Ruf et al. 1994). TMR operates at 18.0, 21.0, and 37.0 GHz with a nadir-viewing geometry. The TBs were calibrated using upward-looking ground-based microwave water vapor radiometers (Keihm and Ruf 1995), DMSP SSM/I observations of the Amazon, and a model of the coldest open ocean brightness temperatures. The path delays were validated using RaOb profiles and the path delay field generated from a numerical weather prediction model. The uncertainty of the TMR open ocean brightness temperature measurement is estimated to be ±1.5 K and the uncertainty of the TMR path delay measurement is demonstrated to be less than 1.1 cm RMS.

A calibration drift in the TMR 18.0 GHz channel was quantified by Ruf (2000) as 0.27 K/year from 1992–1997 and was subsequently accounted for in the TMR data processing algorithms. This analysis was revisited, and it has been determined that the drift did not level off until the middle of 1999. An updated correction for the drift has been implemented by Ruf and Brown (2002). All TMR comparisons in this article use TMR data from 4 February 2002 to 15 August 2002 with the updated drift correction for the TMR 18.0 GHz channel. Also, small yaw-dependent residual biases in the TMR TBs and PDs were identified and removed for this analysis (Brown et al. 2002). TOPEX was moved to a crossing orbit with Jason on 15 August 2002.

Cold TB Calibration—Vicarious Cold Reference

The vicarious cold reference temperature represents a statistical lower bound on brightness temperature for an Earth-viewing radiometer. The vicarious cold reference condition in the microwave, below 90 GHz and away from the 60 GHz oxygen absorption line, occurs under clear skies and calm sea surface conditions with an optimal sea surface temperature that depends on frequency. A method developed by Ruf (2000) is used to determine the vicarious cold reference at each frequency. This method is summarized below.

To determine the theoretical cold reference value, a large data base of modeled TBs was generated by applying a radiative transfer model to radiosonde profiles from 59 open ocean island sites. The data set consisted of over 22,000 profiles from February 2001 through May 2002. A plane parallel radiative transfer model was used with the Stogryn (1971) sea water dielectric model, an updated version of the Liebe (1993) atmospheric water vapor absorption model (Cruz-Pol et al. 1998), and the Rosenkranz (1993) oxygen absorption model to determine the brightness temperature from the RaOb profiles for JMR and TMR frequencies. The 1976 U.S. standard atmosphere was used for heights above the maximum balloon reading, and the SST was set to the temperature of the first reading in the profile. The humidity profile was extrapolated beyond the balloon cut off height, using an exponential fit to the radiosonde's humidity profile. The radiosonde data is acquired from NOAA's Forecast Systems Laboratory (FSL) radiosonde database.

The vicarious cold reference TB is determined from the modeled TB database in the following way. For each frequency, a histogram is formed from the TBs that are within

±10 K of a first guess. The first guess is determined for each frequency by plotting modeled TBs versus SST in dry atmospheric conditions, then choosing the minimum TB. From this histogram, a cumulative distribution function is formed by finding the TB_P for which P percent of the samples in the histogram are less than or equal to that TB_P. In the discrete case, a TB_P is found at even increments of 0.1% in P from 3.0%–10%. A third order polynomial model of the form

$$TB_P = a_{P0} + a_{P1}P + a_{P2}P^2 + a_{P3}P^3, \tag{6}$$

is assumed to represent the cumulative distribution function. The coefficients are found by performing a least-squares regression on the data between 3% and 10%. The vicarious cold reference TB is found by evaluating the resulting function at a frequency of zero (the a_{P0} term). Therefore, the vicarious cold reference represents the highest TB for which there is a zero probability of observing a lower TB.

Given a large modeled data set, a stable vicarious cold calibration reference temperature can be found for each JMR frequency. The accuracy of the vicarious cold reference temperature is dependent on the sea surface emission model used to create the dataset. To mitigate model error in using an absolute cold calibration reference, differences between the vicarious cold reference TBs of adjacent JMR and TMR channels were used to calibrate JMR TBs instead of an absolute JMR cold reference. Thus at the cold end, the JMR TBs will be calibrated using TMR as a standard. This is justified because the TMR TBs are well calibrated (Keihm et al. 2000) and one goal of the calibration is to have no bias between the JMR and TMR PDs.

To find the theoretical difference between the vicarious cold reference at adjacent JMR and TMR frequencies, the vicarious cold reference algorithm was applied to the entire data set of RaOb derived TBs for the three JMR channels and three TMR channels. The difference at adjacent frequencies is the theoretical vicarious cold reference difference. This process was repeated using the Ellison et al. (1998) and Klein and Swift (1976) sea water dielectric models which had minimal impact on the cold reference differences. The maximum deviation of the theoretical cold reference difference found using the other models as compared to the Stogryn model was under 0.1 K for all frequency pairs. The repeatability of the theoretical cold reference difference is determined by finding the cold reference values for 100 random subsets of the 22,000 profiles, and evaluating the standard deviation of the results. Each random subset contained approximately 7,800 profiles. The uncertainty in the cold reference differences is the root-sum-square of the model uncertainty and the repeatability. Table 1 contains the theoretical cold reference differences derived from the RaOb profiles by the method described above. The section Cold TB Calibration Results describes how the JMR TBs are calibrated using the theoretical cold reference differences.

TABLE 1 Theoretical Vicarious Cold References TB Differences Between Adjacent JMR and TMR Channels Calculated Using the Stogryn Emissivity Model (The Uncertainty is the RSS of the Deviation from the Other Surface Emissivity Models and the Repeatability of the Value.)

Theoretical vicarious cold reference TB differences	
JMR 18.7–TMR 18.0	1.59 K ± 0.30
JMR 23.8–TMR 21.0	3.96 K ± 0.61
JMR 34.0–TMR 37.0	−5.61 K ± 0.23

Hot TB Calibration—Amazonian Hot Reference

Suitable geographic regions in the Amazon rainforest were selected as hot TB calibration reference targets. The regions were selected based on the magnitude of the vertically and horizontally polarized TB difference as measured by the SSM/I radiometer at its two window channels of 19.35 and 37.0 GHz. Two regions were chosen where the mean difference between the vertically and horizontally polarized TBs is approximately 1K. The selection criterion locates regions with an optically thick vegetation canopy. In this way, the emission from the surface is reduced from that of a blackbody only by the single scattering albedo of the canopy and is independent of polarization and incidence angle. A method developed by Brown and Ruf (2003), is used to determine the predicted JMR reference TB for each region from SSM/I observations. A summary of the method is given in the appendix.

Comparisons with Coincident Radiosondes

Radiosonde profiles were collected from 59 globally distributed open ocean island launch sites from 15 January 2002 to 15 August 2002 and from 6 April 2003 to 3 August 2003. These dates correspond to JMR cycles 1–24 and 46–55. Generally, the RaObs were launched twice a day. The path delay derived from each profile's humidity and temperature measurements are compared directly to the JMR path delay at the closest approach point. The closest approach points varied from about 4 km to 315 km spatially, and from 0–6 h temporally.

The large data set allowed for several stringent quality control filters. The RaOb profile must reach 10,000 meters, which will ensure a complete sampling of the humidity and temperature profiles. To determine the vapor density at heights above the maximum balloon reading and to flag profiles contaminated by thick clouds, an exponential best-fit of each absolute humidity profile ($\rho_{\mathrm{RaOb}}(z)$) was determined using the model,

$$\rho_{\mathrm{est}}(z) = \rho_0 e^{-\frac{z}{H}}, \tag{7}$$

where $\rho_{\mathrm{est}}(z)$ is the water vapor density, ρ_0 is the water vapor density at the surface, z is the altitude above the surface, and H is the water vapor scale height. The surface water vapor density is determined from the lowest RaOb humidity measurement and the scale height is determined from a least-squares fit of the RaOb humidity profile. To flag for cloudy data, the exponential best fit is required to have an r-squared value of greater than 0.7 as compared to the real profile. The r-squared value is defined as,

$$R^2 = 1 - \frac{\overline{(\rho_{\mathrm{RaOb}} - \rho_{\mathrm{est}})}}{\overline{(\rho_{\mathrm{RaOb}} - \overline{\rho_{\mathrm{RaOb}}})}}, \tag{8}$$

where the overbars represent the mean. It was observed that only a small number of outlier profiles had r-squared values less than 0.7. The closest approach point of the Jason ground track could not be more than 315 km and six hours from the balloon launch. Comparisons are also made with varying bounds on the closest approach point. The variance in the 18.7 GHz brightness temperature of the 10 JMR points surrounding the closest approach point could not be more than 10 K. This minimizes land contamination for points where the radial distance from the island is within JMR's footprint.

The path delay is determined from the radiosonde absolute humidity and temperature profiles. The vapor density profile is determined from the dew point and temperature profile.

The vapor-induced path delay is determined using the relation

$$PD = 1.763 * 10^{-3} \int_0^{\mathrm{TOA}} \frac{\rho_v}{T} dz, \tag{9}$$

where ρ_v is the vapor density [g/m^3], T is the air temperature in K, and dz is in meters. Equation 9 is based on measurements of the wet refractivity component due to water vapor by Boudouris (1963).

JMR Brightness Temperature Calibration Results

The JMR brightness temperatures were calibrated in-flight using TMR comparisons, a vicarious cold reference, and a hot pseudo-blackbody reference. There were noticeable TB calibration offsets just after launch on the order of 1–4 K. There was also a TB offset between the satellite's yaw state. The TBs were generally 2 K higher during the fixed yaw mode as compared to the sinusoidal yaw mode. The yaw offset was readily identified with the colocated JMR and TMR TB and PD data. This is shown in Figure 1.

The TB calibration was corrected by adjusting coefficients included in the Level 1a data processing and the Level 1b data processing, which are the antenna temperature calibration and the antenna pattern correction, respectively. The yaw offset, which was due to a dependence of the TBs on instrument temperature, was corrected by adjusting front-end thermal loss coefficients, specifically K_R and K_{FH} in Equation 1. These coefficients, included in the Level 1a data processing, directly affect any correlation between instrument physical temperature and TB. An initial adjustment was also made to the effective noise diode brightness while tuning K_R and K_{FH} so that the TBs agreed with the vicarious cold reference. The effective noise diode brightness is changed by adjusting the temperature dependence of its brightness. These adjustments had a maximum response at the coldest TBs and minimal affect for the hottest TBs. Further fine tuning of the of TB calibration,

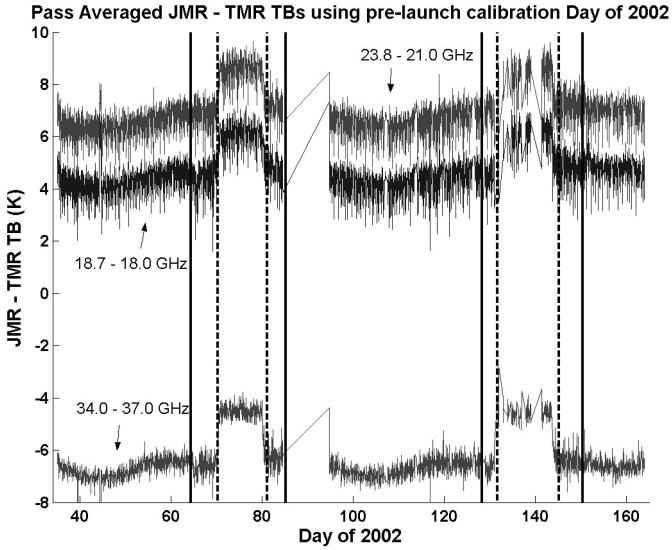

FIGURE 1 Pass averaged JMR–TMR TBs for adjacent channels for JMR cycles 3–21 with the prelaunch calibration coefficients. The JMR (dashed line) and TMR (solid line) yaw transitions are included as vertical lines. Notice the 2 K offset between JMR yaw states.

essentially forcing the TBs to agree with the hot and cold references, was performed by adjusting the off-Earth sidelobe fractions (c-fractions) in the antenna pattern correction (APC) algorithm (Equation 3), which is included in the Level 1b processing. Increasing the c-fractions corresponded to an increase in the brightness temperatures at both ends of the TB range. The increase in brightness temperature was greater for the hottest TBs. Once the TBs were within the uncertainty of the theoretical hot and cold reference values, further adjustments of the c-fractions were performed until no significant bias was observed in the JMR–TMR PD differences. The path delays were then independently verified using the JMR–RaOb path delay differences.

Satellite Yaw State TB Bias

In order for the solar panels to receive the maximum exposure to the sun during allowable ranges of solar beta angles, the satellite periodically changes yaw state from a fixed mode, where the s/c yaw angle is fixed, to a sinusoidal mode, where the yaw angle changes sinusoidally over time. The beta angle is the angle between the orbit plane and a line from the Earth to the Sun. The satellite is in fixed mode for about 10 days and sinusoidal mode for about 30 days as the beta angle varies over its full range. The temperature variation of the instrument hardware is stable to about 2 K while the satellite is in either the sinusoidal or fixed yaw mode. During the transition from one yaw mode to another, the thermal temperature of the instrument hardware changes by about 13 K over a period of 12–15 hours (Figure 2) and temperature gradients develop between the hardware components exposed to the space environment and the internal components. This complex thermal environment could not be simulated during preflight thermal/vacuum testing, leading to a residual correlation between JMR–TMR brightness temperature differences and instrument temperature. This residual correlation was removed by selecting JMR–TMR TB and PD differences 12 hours before and after a yaw transition and adjusting the JMR front-end loss coefficients (K_R and K_{FH}, in Equation 1) until there were no jumps in the differences.

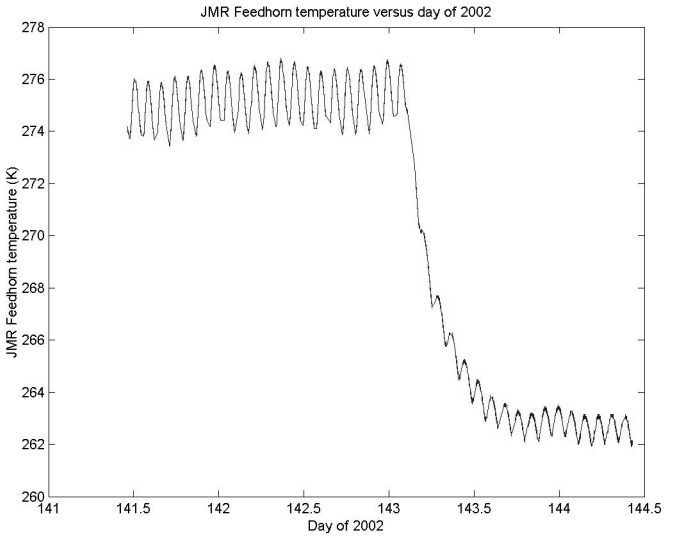

FIGURE 2 Physical temperature of the JMR feedhorn 1 during a yaw transition. Notice the temperature is stable to 2 K away from the transition.

TABLE 2 JMR–TMR Vicarious Cold Reference Differences After Adjusting the Calibration Coefficients

JMR–TMR vicarious cold reference TB differences (Cycles 3–20)	
JMR 18.7–TMR 18.0	1.60 K ± 0.28
JMR 23.8–TMR 21.0	4.02 K ± 0.58
JMR 34.0–TMR 37.0	−6.09 K ± 0.32

Cold TB Calibration Results

It is essential that the JMR TBs are properly calibrated at the low end of the TB spectrum because roughly 50% of the open ocean TBs are within 15 K of the cold reference at 18.7 and 34.0 GHz. The differences between the JMR and TMR cold reference TBs at adjacent channels are required to agree with the theoretical cold reference differences, as discussed previously. The observed cold reference differences after calibration are presented in Table 2. The JMR–TMR cold reference differences in Table 2 represent the average and standard deviation of the differences for cycles 3 through 20. The observed cold reference differences agree with those predicted by theory within their respective uncertainties.

Since a relative calibration reference is used for the cold TB calibration, it is prudent to check that the JMR vicarious cold TBs also agree with the absolute theoretical cold reference value. The uncertainty of the theoretical cold reference TB is given as the root-sum-square of the repeatability of the value and the deviation of the cold reference TB determined using the Stogryn (1971) sea water dielectric model from those using the Ellison et al. (1998) and Klein and Swift (1976) dielectric models. The maximum deviation of the theoretical cold reference TB using the other models from the cold TB found using the Stogryn model was about 0.5 to 0.9 K for the three JMR channels.

The JMR vicarious cold TBs were found for JMR cycles 3–21. This is presented in Table 3. The JMR vicarious cold TBs are all within the uncertainty of the absolute vicarious cold reference. The vicarious cold reference TBs can also be used to detect calibration drifts over time. Long term monitoring of the JMR cold TBs over time scales of years is advisable in order to assess the long term stability of the instrument calibration, in general, and the noise diodes, in particular.

Hot TB Calibration Results

Two regions in the Amazon were used as hot calibration references. Region 1 is 5°–10°S and 65°–74°W and region 2 is 1°S–4°N and 53°–59°W. Table 4 shows the magnitude of the SSM/I-measured vertical and horizontal polarization TB difference averaged over the

TABLE 3 Comparison of the Absolute Vicarious Cold Reference Calculated Using the Stogryn Emissivity Model with JMR Vicarious cold TBs for Cycles 3–21. (The Uncertainty is the RSS of the Deviation from the Other Surface Emissivity Models and the Repeatability of the Value.)

	Absolute theoretical cold reference TBs	JMR vicarious cold TBs for cycles 3–21
18.7 GHz	125.94 ± 1.00 K	125.50 ± 0.32 K
23.8 GHz	135.78 ± 1.03 K	136.01 ± 0.65 K
34.0 GHz	148.72 ± 1.13 K	147.51 ± 0.41 K

TABLE 4 Statistics of the V-pol–H-pol TB Difference from SSM/I Data for Jan.–Sep. 2002 Over two Heavily Vegetated Regions of the Amazon Rainforest (Region 1 is 5°–10°S and 65°–74°W and Region 2 is 1°S–4°N and 53°–59°W

Abs(V-pol minus H-pol) TB	Region 1	Region 2
19.35 GHz	Mean: 0.9198 K	Mean: 0.7636 K
	St. dev.: 0.6717 K	St. dev.: 0.5767 K
37.0 GHz	Mean: 1.0115 K	Mean: 0.8011 K
	St. dev.: 0.7258 K	St. dev.: 0.5785 K

regions at 19.35 and 37.0 GHz. The small (∼1 K) V-pol minus H-pol TB differences indicate that the chosen Amazon reference regions are emitting essentially as black bodies.

The SSM/I observations from F13, F14, and F15 platforms were converted to JMR reference TBs using the methods described in the appendix. Table 5 shows the reference TBs from all three platforms and the average values across the platforms. The averages in Table 5 represent SSM/I overpass data from 4 February 2001 through 15 August 2001, which corresponds to the start of JMR cycle 3 through the end of JMR cycle 21. Each platform has morning and evening local overpass times. The average of all the platforms consists of six local times (6, 8, 10, 18, 20, 22 LST). A large JMR time series, the cycle 3–21 average, was used for comparison to get an adequate sampling of data and local overpass times. The average calibrated JMR TBs over the same regions and same time period are presented in Table 6. The JMR TBs are within ∼0.5 K for the 23.8 and 34.0 GHz channels. The 18.7 GHz hot TBs are 1.6 K lower than the reference, but this has little affect on the retrieved path delays since most of the open ocean TBs are near the cold calibration point.

JMR Wet Path Delay Validation

Results of Comparison with TMR PDs

The availability of TMR in an identical orbit, with only 70 seconds of separation from JMR, allows for unprecedented accuracy in the intercalibration of the JMR and TMR path delay measurements. TMR has been extensively calibrated against various sources of ground truth and has been demonstrated to have PD accuracy of 1.1 cm (Keihm et al. 2000). The initial comparison with TMR showed that JMR was biased 8–12 mm, JMR low. There was also a large PD scale error. The path delay bias was approximately 15 mm, JMR low, for dry

TABLE 5 JMR Hot TB Calibration References Derived from SSM/I Platforms F13, F14, and F15 Over Region 1 and 2 (F13 is at Local Time 6 and 18, F14 is at 8 and 20, and F15 is at 10 and 22. Data is from February Through August of 2002, JMR Cycles 3–21.)

	Nadir hot reference TB (Region 1/Region 2) (K)		
Local time	18.7 GHz	23.8 GHz	34.0 GHz
6, 18	285.0/285.6	284.3/284.4	281.0/281.4
8, 20	286.6/287.1	285.5/285.6	282.8/283.3
10, 22	287.7/287.8	286.7/286.3	283.4/283.4
Average over time and region	286.6	285.5	282.6

TABLE 6 The Average JMR TBs Over Region 1 and 2 in the Amazon Rainforest for JMR Cycles 3–21 After Calibration (Data Represents all Local Times.)

JMR hot TBs averaged over time and region (K)	
18.7 GHz	285.0
23.8 GHz	285.1
34.0 GHz	282.0

atmospheric conditions (JMR PDs less than 10 cm). The bias was approximately 5–7 mm, JMR low, for JMR PDs greater than 10 cm. There were also 2 mm jumps between JMR yaw states due to the TB yaw dependent bias. These jumps were readily identified due to the coaligned orbit of JMR with TMR.

After the JMR TBs were calibrated as discussed the JMR PDs had almost no bias with the TMR PDs in wetter conditions, specifically for PDs greater than 10 cm. There was a residual PD scale error of 5 mm for dry atmospheric conditions. It was realized that the lowest JMR PDs were approximately 1–2 cm lower than the lowest TMR PDs. The lowest JMR PDs were consistently below 1 cm, which, even under the driest conditions, is not physically probable. During cal/val, small modifications were made to the JMR wet troposphere correction algorithm coefficients to improve comparisons with TMR for the driest conditions. As it turned out, the low-end bias was an artifact of an error in the JMR ground system processing software which has since been corrected. The differences in retrieved path delays between the prelaunch and post-cal/val path delay algorithms are very small ($\sim$0.06 cm), and nearly constant over the full range of conditions encountered.

The following results were obtained after the TB calibration and correction of the PD algorithm processing error. Table 7 presents the average JMR–TMR (collocated, 1-second) PD bias over low, medium and high PD ranges along with the RMS of the difference. There is a negligible PD bias between calibrated JMR and TMR PDs and no scale error. The average JMR–TMR PD bias over cycles 3 through 21 is -0.021 cm. Figures 3 and 4 show plots of pass averaged JMR–TMR PD biases. Figure 3 is a plot of the PD difference for the entire PD range. JMR and TMR yaw transition times are represented by vertical lines. It is evident from Figure 3 that there is no offset with yaw state. Figure 4 is a plot of the PD difference for low, medium and high PD values. There is a near zero bias from cycles 3–20 over all PD ranges.

RaOb Validation Results

The JMR PDs were also validated using path delays derived from Radiosonde profiles of the atmosphere. This comparison was done using JMR cycles 1–24 and 46–55. The larger

TABLE 7 The Average JMR–TMR 1-Second PD Differences Averaged Over Cycles 3–21 for Low, Medium, High, and All Path Delay Bins (The RMS Error is Included.)

JMR–TMR PD for cycles 3–21	Mean	RMS
JMR PD $<$ 10 cm	-0.050 cm	0.435 cm
10 cm $\geq$ JMR PD $<$ 20 cm	-0.035 cm	0.429 cm
JMR PD $>$ 20 cm	0.019 cm	0.575 cm
All PDs	-0.021 cm	0.488 cm

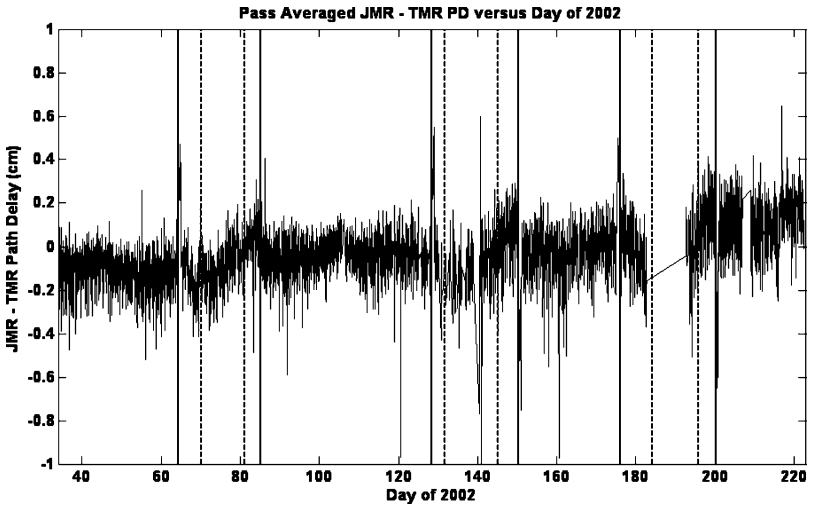

FIGURE 3 Plot of the pass averaged JMR–TMR PD difference versus day of 2002. The JMR (dashed line) and TMR (solid line) yaw transitions are included as vertical lines. Notice there is no significant bias with yaw transition.

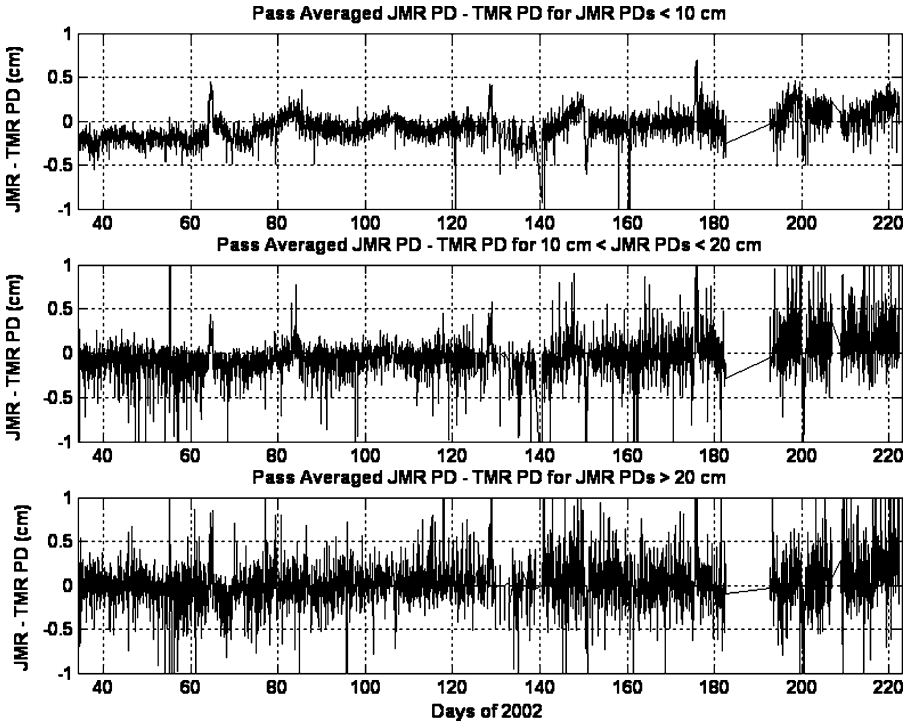

FIGURE 4 Plot of pass averaged JMR—TMR PD differences versus day of 2002 for low (top), medium (middle), and high (bottom) path delay bins. There is no significant scale error evident.

TABLE 8 Mean and RMS of the JMR–RaOb PD Differences for Varying Weather Conditions and Spatial and Temporal Separations (There Does not Appear to be a Bias with Different Cloudy or Windy Conditions.)

Liquid (μm)	Wind (m/s)	Spatial (km)	Temporal (hrs)	Mean (cm)	RMS (cm)	Samples
All Liquid	All Wind	$\leq$315	$\leq$6	0.10	3.05	1722
All Liquid	All Wind	$\leq$150	$\leq$3	0.019	2.52	291
All Liquid	All Wind	$\leq$75	$\leq$1	0.072	1.84	38
$<$75	All Wind	$\leq$315	$\leq$6	$-$0.04	3.09	1302
75 $<$ liq $<$ 300	All Wind	$\leq$315	$\leq$6	0.60	2.88	355
$>$300	All Wind	$\leq$315	$\leq$6	0.14	2.15	5
All Liquid	$<$7	$\leq$315	$\leq$6	$-$0.18	3.14	793
All Liquid	7 $<$ wind $<$ 13	$\leq$315	$\leq$6	0.32	2.92	820
All Liquid	$>$13	$\leq$315	$\leq$6	0.71	2.85	49
$<$75	All Wind	$\leq$200	$\leq$3	0.07	2.74	439
75 $<$ liq $<$300	All Wind	$\leq$200	$\leq$3	0.05	2.34	144
$>$300	All Wind	$\leq$200	$\leq$3	—	—	0
All Liquid	$<$7	$\leq$200	$\leq$3	0.09	2.74	183
All Liquid	7 $<$ wind $<$ 13	$\leq$200	$\leq$3	0.04	2.34	189
All Liquid	$>$13	$\leq$200	$\leq$3	0.35	2.16	11

data set allowed for a better representation of the statistics. JMR is required to retrieve accurately the path delay under windy and cloudy conditions. This can be validated by using the integrated liquid water and surface wind speed estimates that are derived from JMR TBs. The accuracy of the liquid water and wind speed estimates have not been independently validated for this study, but they are adequate to separate the data into different weather groups. The RMS accuracy and mean JMR–RaOb PD differences are shown in Table 8 for various cloudy and windy conditions, as well as various spatial and temporal separation bounds. The mean bias is 0.1 cm with a RMS accuracy of 3.05 cm for all conditions, with 315 km and six hours as the bounds on the closest approach point. The RMS difference between JMR and RaOb PDs drops as the closest approach bounds become tighter. The RMS accuracy of the retrieval is also not affected by varying cloudy or windy conditions and there does not appear to be any significant bias under the varying weather conditions. The JMR PD error is estimated from the RMS values of the RaOb comparison. This is described in a following section.

The comparison with TMR PDs indicated no scale error with path delay. This is also independently confirmed from the RaOb comparison. Table 9 gives the mean and RMS difference between JMR and RaOb PDs for low, medium and high PD values for two different closest approach bounds. There appears to be no significant scale error evident from the RaOb comparisons.

JMR PD Performance

JMR/TMR Error Analysis

The final tuning of the calibration, once the TBs were within the uncertainty of the theoretical hot and cold reference values, was performed until no significant mean bias was observed in the JMR–TMR PD differences. The RMS of the difference between the JMR and TMR

TABLE 9 JMR–RaOb PD Differences for Low, Medium, and High PD Bins for Two Closest Approach Separations (There Does Not Appear to be a Scale Error Present.)

JMR PD (cm)	Spatial (km)	Temporal (hrs)	Mean (cm)	RMS (cm)	Samples
PD < 10	≤315	≤6	0.17	1.83	220
10 ≤ PD < 25	≤315	≤6	−0.15	3.11	627
≥25	≤315	≤6	0.26	3.22	815
PD < 10	≤200	≤3	0.41	1.55	56
10 ≤ PD < 25	≤200	≤3	−0.16	2.52	160
≥25	≤200	≤3	0.20	2.79	167

PDs can be explained by a combination of correlated and uncorrelated sources of error. Error sources that are completely correlated will not affect the RMS differences. Sources of error that are completely uncorrelated will contribute maximally to the RMS difference. Only a fraction of the error from partially correlated sources will affect the RMS difference.

The error sources in the retrieved path delay values for each instrument are due to error in the antenna temperature calibration, error in the antenna pattern correction, and error in the wet tropospheric path delay retrieval (Equations 1, 3 and 5). The error analysis of the antenna temperature calibration is adapted from Ruf et al.'s (1995) TMR TA error budget, the error in the antenna pattern correction from Janssen et al.'s (1995) TMR TB error budget, and the error in the wet tropospheric path delay retrieval from Keihm et al.'s (1995) TMR PD error budget.

The uncorrelated source of error in the antenna temperature calibration (ΔT_A) is due to the stochastic noise of each receiver. The RMS difference between the JMR and TMR PDs should be dominated by the stochastic noise of the receivers. The stochastic noise is estimated to be 0.20 K for each JMR channel and 0.27 K for each TMR channel (Ruf et al. 1995). The JMR stochastic noise value was estimated by finding the RMS of the difference of adjacent 1-second JMR measurements over dry, cloud-free ocean scenes. The error in the TB (ΔT_B) for each channel due to the stochastic noise (ΔT_A) is estimated by its effect in the APC algorithm. Equations for determining the magnitude of the error incurred in the APC algorithm can be found in Janssen et al. (1995). These errors are given in Table 10. The error in the path delay retrieval from the stochastic noise is estimated by the TB error's effect in the path delay retrieval algorithm. This can be estimated using a simplified global average version of the retrieval algorithm for both instruments, given as Equation 10. The coefficients in equations 10 a, b are the c_{18}, c_{23}, and c_{34} coefficients in Equation 5 for global average values of surface wind speed and PD (approximately 7 m/s and 15 cm). The RMS

TABLE 10 Error in the TBs Due to the Stochastic Noise of the Receivers

Channel	ΔTB (K)
TMR 18.0	0.27
JMR 18.7	0.21
TMR 21.0	0.27
JMR 23.8	0.21
TMR 37.0	0.27
JMR 34.0	0.22

difference between the instruments is then the RSS of the PD error for each instrument, as given by

$$\Delta PD_{\mathrm{TMR}} = \{(0.48 * E(TB_{18.0}))^2 + (0.73 * E(TB_{21.0}))^2 + (0.08 * E(TB_{37.0}))^2\}^{\frac{1}{2}}, \tag{10a}$$

$$\Delta PD_{\mathrm{JMR}} = \{(0.41 * E(TB_{18.7}))^2 + (0.65 * E(TB_{23.8}))^2 + (0.19 * E(TB_{34.0}))^2\}^{\frac{1}{2}}, \tag{10b}$$

$$\Delta PD_{\mathrm{JMR-TMR}} = \left\{\Delta PD^2_{\mathrm{JMR}} + \Delta PD^2_{\mathrm{TMR}}\right\}^{\frac{1}{2}}. \tag{10c}$$

The RMS difference between the JMR and TMR PDs explained by the stochastic noise of the receivers is 0.39 cm. The total RMS difference between the JMR and TMR PDs from cycles 3–20 found earlier is 0.49 cm. The remaining RMS difference between the JMR and TMR PDs not explained by the stochastic noise is 0.29 cm, which can be explained by other sources of error.

Other sources of error that can contribute to the RMS difference in the PDs are the uncertainty in the on-Earth sidelobe brightness temperature (ΔT_E) and the spatial and temporal decorrelation between the JMR and TMR measurements. The remaining 0.29 cm in the RMS difference is divided among these sources of error. The maximum spatial separation between the collocated JMR and TMR measurements is about 7 km, which corresponds to a decorrelation error of less than 0.1 cm. This was estimated from Figure 5, which shows spatial decorrelation of PD. This figure is explained in the next section. The 70 seconds of temporal decorrelation between the PD measurements contribute very little to the RMS difference. The on-Earth sidelobe brightness temperatures (T_E) that

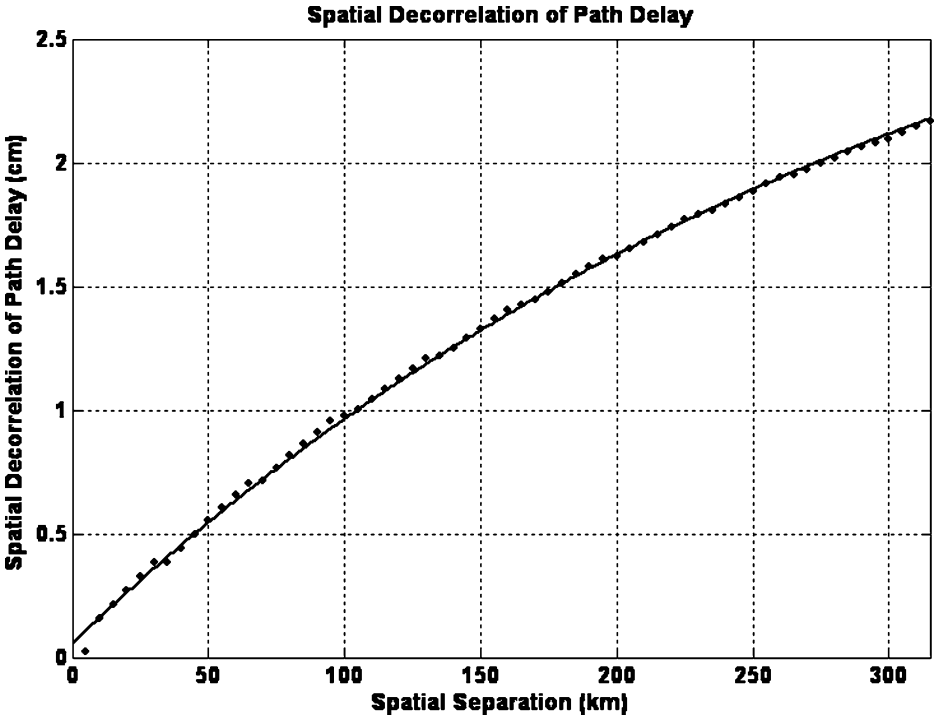

FIGURE 5 Plot of the spatial decorrelation of path delay calculated from JMR PD values.

are used in the APC algorithm (Equation 3) are determined differently for each instrument. The JMR T_E value is determined using a quadratic function of the antenna temperatures, and the TMR T_E value is determined from a look-up table based on frequency and latitude. Some of the remaining RMS difference between the PDs can be explained by the difference in the T_E values. Together these sources of error should explain the remaining 0.29 cm of RMS difference that is not explained by the stochastic noise of the receivers.

The JMR in-flight calibration has produced collocated JMR and TMR PD measurements that have no significant bias or scale error. The RMS difference between the PD measurements is largely explained by the stochastic noise of each receiver. Other sources of error, such as the difference in the on-Earth sidelobe brightness and the spatial decorrelation between the measurements, have minor contributions to the RMS difference. As a whole, the sources of error discussed in this section should explain the 0.49 cm RMS difference between the JMR and TMR PD measurements over cycles 3–21.

JMR/RaOb Error Analysis

The uncertainty of the JMR PD retrieval can also be estimated by comparison to coincident RaOb PDs. The RMS difference between JMR and RaOb PDs is a function of the error in the RaOb PD measurements, the spatial and temporal decorrelation between the two points, and the error in the JMR PD retrieval, as described by

$$RMS_{\mathrm{JMR-RaObPD}}(dist, time) = \sqrt{\Delta RaOb^2 + \Delta JMR^2 + \Delta Spatial(dist)^2 + \Delta Temporal(time)^2}. \quad (11)$$

The spatial and temporal decorrelation terms in Equation 11 can be estimated using statistics from satellite or ground measurements, but the uncertainty in that estimate is unsatisfactory for our purposes. For example, a 5% uncertainty in the spatial decorrelation term will cause a 17% uncertainty in the estimate of the JMR PD error. Figure 5 shows a plot of the cumulative spatial decorrelation (RMS_{PD} ($dist$)) of path delay as a function of separation distance. This was estimated by forming a data set of path delay differences as a function of separation from N JMR PD measurements. Then the cumulative spatial decorrelation at $dist$ km is equal to the RMS of the PD differences with spatial separations from 0 km to $dist$ km, shown in Equation 12.

$$\Delta Spatial(dist) \cong RMS_{PD}(\mathrm{dist}) = \left[\frac{1}{N} \sum_{i=1}^{i=N} \frac{1}{\max(j)} \sum_{\Delta r=0}^{\Delta \mathrm{r=dist}} [PD_i(r_0) - PD_j(r_0 + \Delta r)]^2 \right]^{\frac{1}{2}}. \quad (12)$$

A least-squares regression of the cumulative spatial decorrelation (Equation 12) was fit to the data. An exponential function of the form

$$RMS_{PD}(dist) = c_{\mathrm{RMS0}} - c_{\mathrm{RMS1}} \exp\left(-\frac{dist}{c_{\mathrm{RMS2}}}\right) \quad (13)$$

is used, which is reasonable because the spatial decorrelation should asymptotically approach a constant value at large spatial separations. The least-squares best fit of the spatial

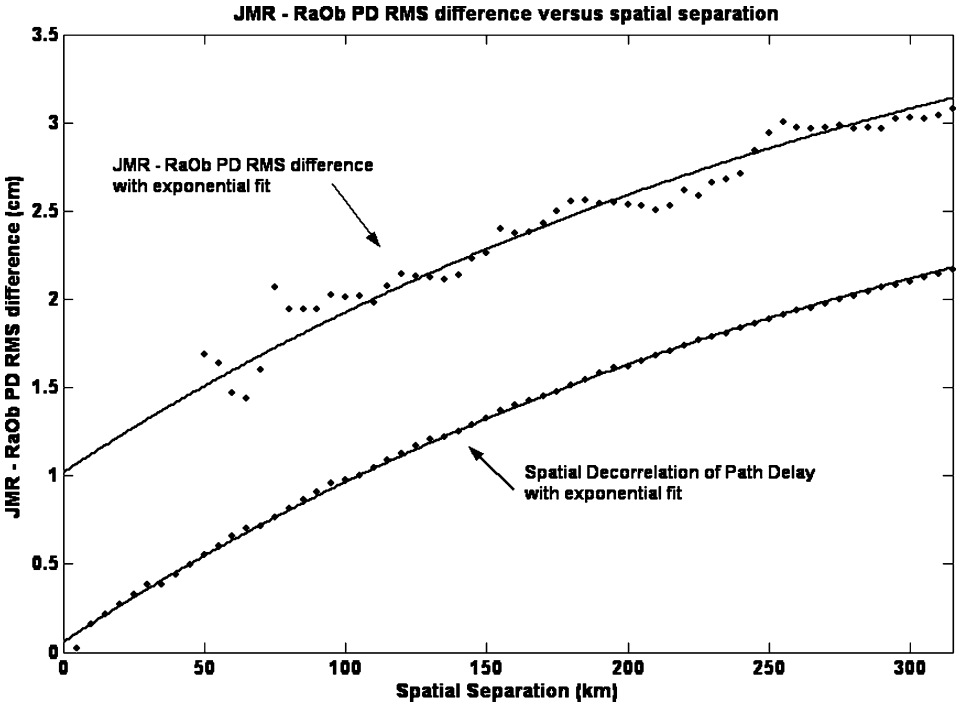

FIGURE 6 Plot of the JMR–RaOb PD RMS difference versus spatial separation (with minimal temporal separation). A plot of the spatial decorrelation of path delay is included for comparison. An exponential fit is applied to the JMR–RaOb PD RMS difference that has a constant offset from the exponential fit of the spatial decorrelation.

decorrelation gives $c_{\mathrm{RMS0}} = 3.46$, $c_{\mathrm{RMS1}} = 3.40$, and $c_{\mathrm{RMS2}} = 322.41$. There is a small offset from zero, 0.6 mm, which is most likely due to the stochastic noise in the JMR TB measurements. We should expect a plot of JMR–RaOb RMS difference (Equation 11) as a function of separation distance (with minimal temporal separation) to have a similar shape with a constant offset that is equal to the RSS of the remaining error terms. This suggests a more robust way to estimate the JMR PD error term.

Figure 6 shows a plot of JMR–RaOb RMS difference versus spatial separation with less than 45 minutes of time separation. The data is grouped by spatial separations of 50 through 315 km in 5 km increments. Each point represents the RMS difference of the data with separation distances less than or equal to the current increment. For example, the data point at 200 km is the RMS difference of all data for which the closest approach point is less than or equal to 200 km. Only data with separation distances greater than 40 km are used, because this is the nominal size of the JMR footprint. The land contamination in the TB values causes the RMS PD error to increase dramatically with separation distances less than the JMR footprint size. The spatial decorrelation of path delay (from Figure 5) is included in this plot for comparison.

A least-squares fit is found for the JMR–RaOb RMS PD difference using (Equation 13) with $c_{\mathrm{RMS1}} = 3.40$, and $c_{\mathrm{RMS2}} = 322.41$. This gives $c_{RMS0} = 4.42$. The JMR–RaOb RMS PD difference at zero spatial separation (with minimal temporal separation) is 1.02 cm. The uncertainty associated with this value is ± 0.1 cm. This was determined by finding the standard deviation of the residual between the least-squares fit and the JMR–RaOb RMS PD difference.

The uncertainty of the JMR PD can be determined by subtracting the RaOb error from the estimate of RMS PD difference at zero spatial separation (with minimal temporal separation). The uncertainty in the radiosonde humidity profile is estimated to be 0.7 cm (Alishouse et al. 1990). This is most likely a conservative estimate, but it will be used because a higher value will decrease the estimated JMR PD error. Also, this is the radiosonde error estimate that was used to determine the uncertainty of the TMR PD measurement, so it will allow for easy comparisons of the PD uncertainty of the two instruments. Using this estimate, Equation 11 is used to determine the uncertainty of the JMR PD measurement. The RMS error estimate of 1.02 cm from Figure 6 has error bars of approximately ± 0.1 cm. Thus the uncertainty of the 1-second JMR PD measurement is estimated to be 0.74 cm $\pm$ 0.15 cm. The uncertainty in the JMR PDs is better than the 1.2 cm mission requrement.

Summary and Conclusions

The Jason Microwave Radiometer is included on the Jason-1 Ocean Altimetry satellite to measure the wet tropospheric path delay of the altimeter signal. Accurate retrieval of the path delay values requires well-calibrated brightness temperatures and a precise inversion algorithm. The JMR TBs are calibrated on-orbit over the entire dynamic range of the instrument. The TBs are calibrated at the cold end of the TB range by using a vicarious cold reference, which represents a statistical lower bound on brightness temperature. The TBs are calibrated at the hot end of the TB range using hot reference TBs determined from SSM/I over heavily vegetated regions of the Amazon rainforest.

The retrieved path delay values are validated using collocated TMR and RaOb derived PD values. There is no significant bias between the JMR and TMR PDs and no error that scales with path delay. This is also confirmed independently by the comparison with the RaOb derived PD values. There are no noticeable biases in cloudy or windy conditions between the JMR and RaOb PDs and no scale errors.

The uncertainty of the JMR PD measurement can be estimated in two ways. First, the RMS difference between the JMR and TMR PDs is largely explained by the stochastic noise of the recievers, and the remaining difference is explained by the difference in the on-Earth sidelobe brightness used in the APC and the spatial decorrelation of the measurement. The uncertainty in the JMR PDs can also be estimated from the RaOb PD comparisons. The RMS difference between the JMR and RaOb PDs is a function of the RaOb error, JMR error, and the spatial and temporal decorrelation between them. The RMS difference is extrapolated to zero spatial separation at minimum temporal separation. The error in the RaOb measurement is removed from the remaining RMS difference, leaving only effects of the JMR PD error. The uncertainty of the JMR PD measurement is estimated to be 0.74 cm $\pm$ 0.15.

References

Alishouse, J. C., S. A. Snyder, J. Vongsathorn, and R. R. Ferraro. 1990. Determination of oceanic total precipitable water from SSM/I. *IEEE Trans. Geosci. Rem. Sensing* 28:811–816.

Boudouris, G. 1963. On the index of refraction of air, the absorption and dispersion of centimeter waves by gasses. *J. Res. Natl. Bur. Stand. Sect. D*. 67: 631–684.

Brown, S., and C. Ruf. 2003. On-orbit microwave blackbody calibration using regions of dense vegetation. *IGARSS 2003 Conf. Proc.*

Brown, S., C. Ruf, and S. Keihm. 2002. Brightness temperature and path delay correction for TOPEX microwave radiometer yaw state bias. *Technical Memo*, 8 August 2002.

Cruz-Pol, R. C. Ruf, and S. Keihm. 1998. Improved 20–32 GHz atmospheric absorption model. *Radio Sci*. 22(5):1319–1333.

Ellison W., A. Balana, G. Delbos, K. Lamkaouchi, L. Eymard, C. Buillou, and C. Prigent. 1998. New permittivity measurements of seawater. *Radio Sci.* 33(3):639–648.

Jason-1 Project. 2001. *AVISO and POCAAC User Handbook*, IGDR and GDR Jason Products. Ed. 1.0. JPL D-21352 (PODAAC).

Janssen, M., C. Ruf, and S. Keihm. 1995. TOPEX/Poseidon microwave radiometer (TMR): II. antenna pattern correction and brightness temperature algorithm. *IEEE Trans. Geosci. Rem. Sensing* 33(1):138–146.

Keihm S., and C. Ruf. 1995. Role of water vapor radiometers for in-flight calibration of the TOPEX microwave radiometer. *Mar. Geod*. 18:139–156.

Keihm, S. J., M. A. Janssen, and C. S. Ruf. 1995. TOPEX/Poseidon microwave radiometer (TMR): III. Wet troposphere range correction algorithm and pre-launch error budget. *IEEE Trans. Geosci. Rem. Sensing* 33(1):147–161.

Keihm, S. V. Zlotnnicki, and C. Ruf. 2000. TOPEX microwave radiometer performance evaluation 1992–1998. *IEEE Trans. Geosci. Rem. Sensing* 38(3):1379–1386.

Kitiyakara, Ami. 2002. JMR T/V Calibration. *JPL Interoffice Memorandum*. January 25, 2002.

Klein L. A., and C. T. Swift. 1976. An improved model for the dielectric constant of sea water at microwave frequencies. *IEEE Trans. Ant. Propogat*. 25:104–111.

Liebe, H. J., G. A. Hufford, and M. G. Cotton. 1993. Propagation modeling of moist air and suspended waterlice particles at frequencies below 1000 GHz. AGARD Conf. Proc. 542. 3-1-3-10.

Menard, Y., and B. Haines. 2001. Jason-1 CALVAL Plan. Reference Project: TP2-J0-PL-974-CN. JPL Document. April 2, 2001.

Rosenkranz, P. 1993. Absorption of microwaves by atmospheric gases. In *Atmospheric Remote Sensing by Microwave Radiometry,* Ch. 2. M. Janssen (ed). New York: Wiley.

Ruf, C. S. 2000. Detection of calibration drifts in spaceborne microwave radiometers using a vicarious cold reference. *IEEE Trans. Geosci. Remote Sensing* 38(1):44–52.

Ruf, C., and S. Brown. 2002. Topex microwave radiometer 18 GHz drift—Revisited. 29 May 2002 Technical memo submitted to Jason-1 project.

Ruf, C., S. Keihm, B. Subramanya, and M. Janssen. 1994. TOPEX/Poseidon microwave radiometer performance and in-flight calibration. *J. of Geo. Res.* 99(C12):24,915–24,926.

Ruf, C. S. Keihm, and M. Janssen. 1995. TOPEX/Poseidon Microwave Radiometer (TMR): I. Instrument description and antenna temperature calibration. *IEEE Trans. Geosci. Rem. Sensing* 33(1):125–137.

Stogryn, A. 1971. Equations for calculating the dielectric constant of saline water. *IEEE Trans. on Microwave Theory and Techniques* 733–736.

Stum, J., P. Vincent, S. Desai, F. Parisot, and S. Coutin-Faye. 2001b. Algorithm definition, accuracy and specification, Volume 3. CMA Radiometer level 1B processing. Reference project: SMM-ST-M2-EA-11004-CN. Issue 3. Update 2. CNES SSALTO document.

Stum, J., J. Zigna, S. Desai, A. Kitiyakara, and T. Pavlovitch. 2001a. CCI JMR Level 1.0 Processing. Reference project: SMM-ST-M1-EA-11577-CN. Issue 3. Update 0. CNES SSALTO document.

F. Ulaby, R. Moore, and A. Fung. 1982. *Microwave remote sensing, active and passive. Volume II: Radar remote sensing and surface scattering and emission Theory* pp. 887–894, Dedham, MA: Artech House.

F. Ulaby, R. Moore, and A. Fung. 1986. *Microwave remote sensing, active and passive. Volume III: From Theory to Applications* pp. 1413–1467. Dedham, Massachussetts: Artech House.

Westwater, E. 1993. Ground-based microwave remote sensing of meteorological variables. In *Atmospheric remote sensing by microwave radiometry*, M. Janssen (ed). New York: Wiley.

Appendix: Amazonia Blackbody Reference Model Parameterization

Above 10 GHz for regions with an optically thick vegetation canopy, the surface brightness can be modeled as

$$T_{\mathrm{B,canopy}} = (1 - a(f))T_v, \tag{A.1}$$

where $a(f)$ is the single scattering albedo and T_v is the physical temperature of the vegetation (Ulaby et al. 1982). It is reasonable to assume that the albedo varies with frequency, since

the wavelength of the radiation is changing relative to the leaf dimensions. The apparent brightness temperature over these regions can be written as

$$TB_{\text{app}}(f,\theta) = (1 - a(f))T_v e^{-\tau(f)\sec(\theta)} + TB_{\text{up}}(f,\theta) + \Gamma_{\text{scat}}(f)(TB_{\text{down}}(f))e^{-\tau(f)\sec(\theta)}, \quad \text{(A.2)}$$

where θ is the incidence angle, $\Gamma_{\text{scat}}(f)$ represents the fraction of downwelling radiation scattered into θ from the canopy, $TB_{\text{down}}(f)$ represents the hemispherical contribution of the downwelling brightness temperature, $TB_{\text{up}}(f, \theta)$ is the upwelling atmospheric brightness temperature, $TB_{\text{app}}(f, \theta)$ is the main beam brightness temperature at the antenna, and $\tau(f)$ is the zenith optical depth of the atmosphere. The surface contribution can be estimated from SSM/I brightness temperatures by inverting (A.2) and solving for T_v. This requires that $TB_{\text{UP}}(f, \theta)$, $\tau(f)$, $TB_{\text{down}}(f)$, $\Gamma_{\text{scat}}(f)$, and $a(f)$ are known for SSM/I frequencies. These variables can be estimated from the SSM/I data in the following way.

Statistical inversion methods have been used to retrieve atmospheric parameters such as vertically integrated path delay and liquid water, such as the method used to retrieve JMR PD. A similar method is used to find the upwelling TBs. The upwelling brightness temperature at SSM/I frequencies is estimated using a statistical inversion involving the 19.35, 22.235, and 37.0 GHz SSM/I channels. The upwelling TB is written as a linear combination of the lower three channels

$$TB_{\text{UP}}(f, 53^\circ) = c_{\text{UP0}} + c_{\text{UP1}} TB_{\text{app}}(19.35, 53^\circ) + c_{\text{UP2}} TB_{\text{app}}(22.235, 53^\circ) + c_{\text{UP3}} TB_{\text{app}}(37.0, 53^\circ). \quad \text{(A.3)}$$

Using an average atmospheric effective radiating temperature over the Amazon and the SSM/I upwelling TBs determined from (A.3) (Westwater 1993), the zenith integrated optical depth can be determined by

$$\tau(f) = -\ln\left(1 - \frac{TB_{\text{UP}}(f,\theta)}{T_{\text{eff}}(f)}\right)\cos(\theta). \quad \text{(A.4)}$$

The hemispherical downwelling component is the downwelling brightness temperature from the atmosphere and the cosmic background integrated over solid angle. This can be estimated at each SSM/I frequency from the upwelling TB component by

$$TB_{\text{down}}(f) = c_{\text{DN0}} + c_{\text{DN1}} TB_{\text{up}}(f, 53^\circ). \quad \text{(A.5)}$$

The hemispherical downwelling radiation is assumed to be scattered isotropically by the canopy. In this way, $\Gamma_{\text{scat}}(f)$ can be written as $a(f)/2$. It is assumed that the single scattering albedo increases linearly and monotonically from 18–40 GHz, which is represented as

$$a(f) = c_{\text{ao}} + c_{\text{a1}} f. \quad \text{(A.6)}$$

Once the physical temperature of the canopy is determined, the apparent brightness temperatures at JMR frequencies and incidence can be determined if $TB_{\text{UP}}(f, \theta)$, $\tau(f)$, $TB_{\text{down}}(f)$, $\Gamma_{\text{scat}}(f)$, and $a(f)$ are known at JMR frequencies and nadir incidence. A least-squares regression is determined which relates TB_{UP} at SSM/I frequencies to JMR frequencies at adjacent channels. Then $\tau(f)$ is determined using Equation (A.4), TB_{down} is determined

using an equation with the form of Equation (6), and $\Gamma_{\text{scat}}(f)$, and $a(f)$ are determined using equation (A.6).

To determine the coefficients in the above equations, radiosonde data in the vicinity of the selected regions are used to model the apparent TBs, integrated optical depth, effective radiating temperature, and the upwelling and downwelling TBs. RaOb sounding data from October 2001 through September 2002 are used from four stations in the Amazon.

The measured apparent TB data set consists of measurements from October 2001 through September 2002 from the DMSP SSM/I F13, F14, and F15 platforms acquired from Remote Sensing Systems.

The equations are parameterized using a least-squares optimization of the modeled radiosonde database. The dependence of the single scattering albedo on frequency, (A.6), is determined by solving for $a(f)$ in (A.2) using average modeled values for the atmospheric TB components with average SSM/I apparent TBs at 19, 22, and 37 GHz.

Using the paramertization of the above equations, average JMR reference TBs for each channel and each region were determined from nine months of SSM/I data across three platforms (F13, F14, and F15). Each SSM/I satellite is in a sun-synchronous orbit with morning and evening local overpass times. This provides an adequate representation for the daily average of the hot reference temperature for JMR cycles 3–21.